

Bosonic metal states in crystalline iron-based superconductors at the two-dimensional limit

Yanan Li^{1,6#}, Haiwen Liu^{2#}, Shichao Qi¹, Haoran Ji¹, Xiaotong Jiao^{3,5}, Wenfeng Dong³, Yi Sun¹, Wenhao Zhang^{3,8}, Chengcheng Ji¹, Zihan Cui⁴, Minghu Pan⁵, Nitin Samarth⁶, Lili Wang³, X.C. Xie^{1,10,11}, Qi-Kun Xue^{3,11,12}, Yi Liu^{4,7*}, and Jian Wang^{1,9,10,11*}

¹*International Center for Quantum Materials, School of Physics, Peking University, Beijing 100871, China*

²*Center for Advanced Quantum Studies, Department of Physics, Beijing Normal University, Beijing 100875, China*

³*State Key Laboratory of Low-Dimensional Quantum Physics, Department of Physics, Tsinghua University, Beijing 100084, China*

⁴*Department of Physics, Renmin University of China, Beijing 100872, China*

⁵*School of Physics and Information Technology, Shaanxi Normal University, Xi'an 710119, China*

⁶*Department of Physics, The Pennsylvania State University, University Park, Pennsylvania 16802, USA*

⁷*Beijing Key Laboratory of Opto-electronic Functional Materials & Micro-Nano Devices, Renmin University of China, Beijing 100872, China*

⁸*School of Physics and Wuhan National High Magnetic Field Center, Huazhong University of Science and Technology, Wuhan 430074, China*

⁹*Collaborative Innovation Center of Quantum Matter, Beijing 100871, China*

¹⁰*CAS Center for Excellence in Topological Quantum Computation, University of Chinese Academy of Sciences, Beijing 100190, China*

¹¹*Beijing Academy of Quantum Information Sciences, Beijing 100193, China*

¹²*Southern University of Science and Technology, Shenzhen 518055, China*

[#]These authors contribute equally

*Correspondence to: jianwangphysics@pku.edu.cn (J.W.); yiliu@ruc.edu.cn (Y.L.)

The nature of the anomalous metal, one of the quantum ground states of two-dimensional (2D) bosonic systems, remains a major puzzle even after several decades of study. Here, we report a systematic investigation on the transport

properties of ultrathin crystalline FeSe films grown on SrTiO₃ (STO) as well as the nanopatterned FeSe/STO, where the 2D high-temperature superconductivity is confined at the interface. Remarkably, the bosonic anomalous metal state emerges around 20 K, an exceptionally high temperature compared to all previous observations. Furthermore, a linear-in-temperature (*T*-linear) resistance with suppressed Hall coefficient below onset temperature for superconductivity is observed, indicating a bosonic strange metal. We give quantitative analysis for the bosonic anomalous metal state, based on the quantum dynamical property of vortices influenced by ohmic dissipation. This microscopic model pins down the origin of the intriguing anomalous state to the superconducting phase dynamics in both spatial and temporal domain. Our findings shed new light on the bosonic metal states in crystalline superconductors at the 2D limit.

The low-lying fermionic excitations are gapped out in a superconductor when electrons form Cooper pairs and condense into the quantum ground state. Governed by the Heisenberg uncertainty principle, there is phase and particle-number duality of Cooper pairs¹. Thus, zero-resistance superconducting state with phase-coherent Cooper pairs and insulating state with localized Cooper pairs are believed to be the two ground states of two-dimensional (2D) superconductors¹. However, when approaching zero temperature, a saturated finite resistance much smaller than the Drude value is detected, showing an anomalous metal state in 2D superconductor-insulator/metal transitions, which challenges the prevailing consensus^{2,3}. The observation of linear current-voltage (*I-V*) curve further confirms the metallic characteristic. The vanishing Hall coefficient^{4,5} and quantum oscillations with a period of one superconducting flux quantum $\frac{h}{2e}$ (*e* is the electron charge and *h* is the Planck's constant)⁵ in the anomalous metal state suggest that Cooper pairs dominate the transport. The origin of the bosonic feature is still poorly understood^{2,3}, despite the ubiquitous observations of anomalous metal in a variety of 2D superconducting systems since 1989, including amorphous and granular films^{4,6-10}, crystalline films and nanodevices¹¹⁻¹⁷, superconducting arrays^{5,18-20}, and interfacial superconducting systems^{21,22}. Furthermore, other exotic metallic behaviors of the bosonic systems remain unexplored. Compared with the 2D superconducting systems mentioned above, the ultrathin FeSe crystalline films grown

on SrTiO₃ (STO) substrate possess high-temperature superconductivity²³⁻²⁶, which emerges at the FeSe/STO interface and is localized in the first unit-cell FeSe on STO^{24,25}. The 2D nature of superconductivity has been justified by typical Berezinskii-Kosterlitz-Thouless (BKT) transition and the large anisotropy of the upper critical field²⁵. These features make the FeSe/STO a superior platform for the exploration of 2D bosonic metal states and the corresponding dissipation mechanisms.

The vortex dynamics plays a dominant role in the transport characteristics of superconducting systems²⁷. Previous investigations have showed that both the free vortex motion above BKT temperature²⁸ and the thermal activated flux flow²⁹ lead to electric resistance in a bosonic system. The quantum tunneling process of vortices (also named as quantum creep) driven by quantum fluctuations determines the low temperature resistance features²⁷, which can be largely influenced by the ohmic dissipation effect^{30,31}. Meanwhile, the dissipative quantum tunneling provides quantitative understanding³² for the damping rate of phase difference in Josephson junctions³³. The experimental investigations on the quantum behavior of phase difference across a Josephson junction³⁴ have stimulated the long-term pursuit of quantum computation based on superconducting qubits in Josephson junction systems³⁵. The investigations on the bosonic metal states in two-dimensional superconductors may extend the substantial endeavors in the superconducting quantum circuits to form a panoramic paradigm for the emergent phase dynamics under the influence of dissipation effect.

Anomalous metal states in pristine FeSe/STO

In this paper, we report systematic transport measurements on ultrathin crystalline FeSe films down to one unit-cell thickness grown on STO substrates by molecular beam epitaxy. The scanning tunneling microscope (STM) images show tetragonal lattice structure of our FeSe film (Extended Data Fig. 1). For *ex-situ* transport measurements, we grew a series of macroscopic FeSe films (1-5 unit-cells thick) on pretreated insulating STO(001) substrates with protective FeTe capping layers (see Methods). The sheet resistance (R_s) versus temperature (T) curves of FeSe films reveal a superconductor to weakly localized metal transition with increasing normal state resistance (R_N) (Fig. 1a). When R_N is small, superconducting state (sample S1 in Fig. 1a)

and anomalous metal state (sample S2) are observed. Sample S1 (Fig. 1a) shows zero-resistance within the measurement resolution at $T_c^{\text{zero}} = 17.4$ K and the onset superconducting critical temperature $T_c^{\text{onset}} = 46.6$ K (Extended Data Fig. 2b). Here, T_c^{onset} is defined as the temperature where the sheet resistance deviates from the linear extrapolation of the normal state, and the normal state resistance is defined as $R_N = R_s(T_c^{\text{onset}})$. The zero-resistance state fades away in sample S2, accompanied by the appearance of small finite resistance (very close to zero), reminiscent of an anomalous metal state. When R_N increases, the superconducting transition is broadened as shown by samples S3 and S4 in Fig. 1a. For the FeSe film with larger normal state resistance (S5 in Fig. 1a), the sheet resistance increases monotonically down to the lowest temperature. We used the six-probe method to simultaneously measure the Hall (R_{yx}) and longitudinal resistance (R_s) for samples showing anomalous metal states (Fig. 1b and Supplementary Fig. 1). Above the superconducting transition, the small negative Hall coefficient indicates the heavy electron doping in the film, consistent with previous reports³⁶. Below T_c^{onset} , the Hall coefficient (R_{yx}/B , B is the magnetic field) drops with decreasing temperature and reaches zero within the measurement resolution below 20 K while R_s remains finite, indicating that Cooper pairs (bosons) dominate the transport behavior of the metallic states at low temperatures^{4,5}.

Figure 1c presents the Arrhenius plots of the anomalous metal state under different perpendicular magnetic fields. Surprisingly, the anomalous metal state persists up to $T^{\text{AM}} = 19.7$ K (56.1% of T_c^{onset}) at zero magnetic field, which is much higher than previous reports². An external magnetic field up to 15 T in the perpendicular direction (B_{\perp}) broadens the superconducting transition and reduces T^{AM} from 19.7 K to 7.0 K (Fig. 1c). The high-temperature anomalous metal state is confirmed in more FeSe films on STO (Fig. 1d and Extended Data Fig. 3). In previous studies of conventional superconductors, the anomalous metal state only exists over a temperature scale of hundreds of millikelvin^{4,8,11,16-21} (see Fig. 1e). In high-temperature cuprate superconductors (e.g. $\text{La}_2\text{CuO}_{4+\delta}$ and nanopatterned $\text{YBa}_2\text{Cu}_3\text{O}_{7-x}$ films, the open orange circles in Fig. 1e), the anomalous metal state is reported up to ~ 10 K, corresponding to a relatively small ratio of $T^{\text{AM}}/T_c^{\text{onset}}$. A large $T^{\text{AM}}/T_c^{\text{onset}}$ ratio is commonly seen in interface superconductors, however, these systems usually show a low T^{AM} (e.g. LAO/KTO and LAO/STO, the blue diamond dots in Fig. 1e). Therefore,

the extremely high T^{AM} accompanied by the large ratio of $T^{\text{AM}}/T_c^{\text{onset}}$ in ultrathin FeSe films (the open orange diamond in Fig. 1e) are striking in this context.

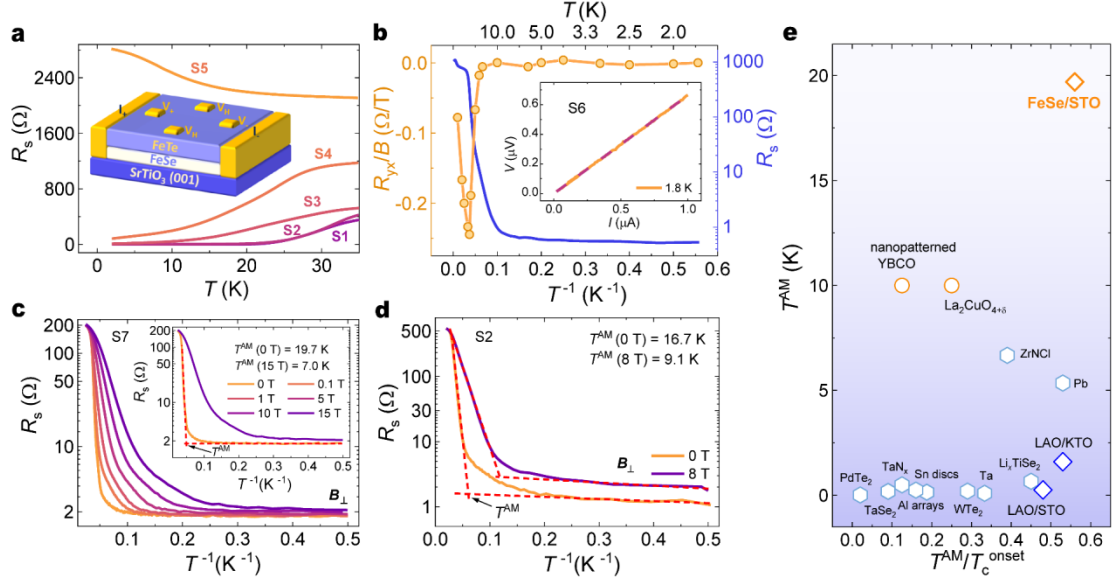


Fig. 1 High-temperature anomalous metal state in FeSe/STO. **a**, Temperature dependent sheet resistance $R_s(T)$ of FeSe/STO sample S1 to S5 with different normal state resistances, showing superconductor-anomalous metal-weakly localized metal transitions. Inset is a schematic for six-probe transport measurements on FeSe/STO. **b**, The $R_s(T)$ curve (the blue curve) and the Hall coefficient R_{yx}/B (the yellow dots) of sample S6. The Hall coefficient goes to zero below 20 K. Inset is an I - V curve at 1.9 K showing a linear behavior below 300 nA. The excitation current for $R_s(T)$ measurements is 100 nA, which is within the ohmic region. **c**, Arrhenius plots of $R_s(T)$ curves under perpendicular magnetic fields, showing an anomalous metal state with onset temperature (T^{AM}) up to 19.7 K (sample S7). T^{AM} is the temperature where anomalous metal state appears, defined as the crossing point of the extrapolation of resistance drop and saturation. **d**, The resistance saturation of the anomalous metal states in sample S2 under perpendicular magnetic fields of 0 T and 8 T. **e**, Overview of T^{AM} and the ratio $T^{\text{AM}}/T_c^{\text{onset}}$ of various 2D superconducting systems, including amorphous and granular films^{4,6,8}, crystalline films and nanodevices^{11,13,14,16,17}, superconducting arrays^{5,19,20}, and interfacial superconducting systems^{21,22}. The FeSe/STO in this paper is indicated by a yellow diamond dot. The highest values of T^{AM} and $T^{\text{AM}}/T_c^{\text{onset}}$ from each 2D superconducting system are shown in this panel.

Bosonic strange metal states in pristine FeSe/STO

In the wide superconducting transition region of FeSe films with a larger normal state resistance, we observe an extraordinary linear-in-temperature resistance below T_c^{onset} . Figure 2 summarizes the T -linear resistance under perpendicular magnetic fields. The T -linear resistance extends to lower temperatures (Fig. 2a, d), and the corresponding temperature regime ($\Delta T/T_c^{\text{onset}}$) grows with increasing magnetic field (Fig. 2b, e) when the field is relatively small. Under a higher magnetic field, T_c^{onset} decreases and the temperature regime of T -linear resistance shrinks. This T -linear resistance behavior is reminiscent of the strange metal state in fermionic strongly correlated systems such as the cuprates³⁷⁻³⁹, pnictides^{40,41}, heavy fermion systems^{42,43}, and magic angle graphene⁴⁴. The fermionic strange metal is associated with the quantum criticality of unconventional superconductivity or magnetism, where pseudogap⁴⁵, nematic order⁴⁶, and ferromagnetic⁴⁷ or antiferromagnetic⁴⁸ order are suppressed. In our measurements, the slopes α_B of T -linear resistance below T_c^{onset} are summarized in Fig. 2c, f. With increasing magnetic field, α_B firstly increases and then decreases, showing opposite behavior to $\Delta T/T_c^{\text{onset}}$ (Fig. 2b, e). At zero field, the slope of the FeSe film is around 34-120 Ω/K , an extremely large value compared with previous observations of fermionic strange metals. To be specific, the slope α_F for high-temperature cuprate superconductors (e.g. $\text{La}_{2-x}\text{Sr}_x\text{CuO}_4$, $\text{Pr}_{2-x}\text{Ce}_x\text{CuO}_{4\pm\delta}$, and $\text{La}_{2-x}\text{Ce}_x\text{CuO}_4$) lies in the range 1.7-8.2 Ω/K ³⁸. Furthermore, recent studies report that α_F is even smaller (~ 0.13 Ω/K) in pulsed-laser deposition grown thick FeSe films⁴⁹. In our measurements, above T_c^{onset} one typical 1-UC FeSe/STO shows T -linear resistance with the slope of 1.23 Ω/K (Extended Data. Fig. 2b). Therefore, a fermionic strange metal state cannot explain the large slope observed in our FeSe films below T_c^{onset} . Additionally, the Hall coefficient is significantly suppressed with decreasing temperature in the temperature regime of T -linear resistance (Supplementary Figs. 1c, d). Thus, the strange metal state below T_c^{onset} mostly originates from the transport of Cooper pairs (bosons) rather than quasiparticles (fermions).

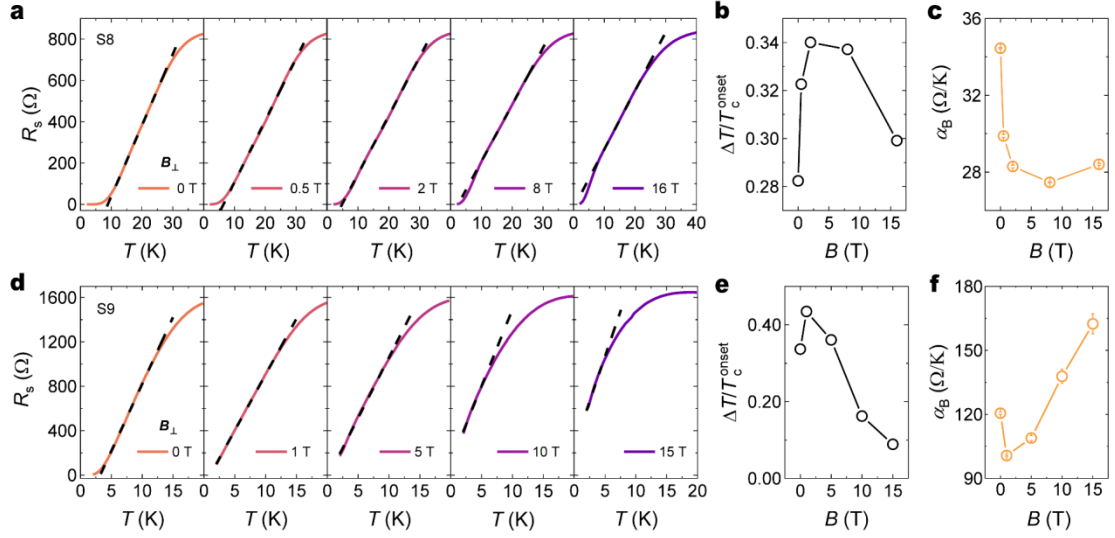


Fig. 2 T -linear resistance of FeSe/STO below T_c^{onset} . **a, d,** The $R_s(T)$ curves (**a** (S8) and **d** (S9)) under perpendicular magnetic fields. The black dashed lines are fits to the linear part of $R_s(T)$ curves, indicating a strange metal state. **b, e,** Field dependence of the temperature ratio ($\Delta T/T_c^{\text{onset}}$), ΔT is the temperature range of the linear $R_s(T)$ curves. **c, f,** The slopes α_B of linear $R_s(T)$ under different fields in **a** and **d**.

Modulation of bosonic metal states via the nano-holes

To further explore the nature of the bosonic metal states in FeSe/STO systems below T_c^{onset} , we tune the disorder strength of FeSe/STO by fabricating a triangular array of nano-holes. Specifically, the superconducting FeSe/STO samples (~ 2 unit-cells of FeSe with FeTe protection layers) are etched through a contact mask via reactive ion etching (RIE) (see Methods for details). The patterns, which have ~ 70 nm diameter holes arranged in a triangular array with center-to-center spacing of ~ 102 nm, are transferred onto the FeSe films (see Extended Data Fig. 4 for a scanning electronic microscope image of the patterns). The intermediate triangular superconducting areas (marked as island in Fig. 3b) between the nano-holes connect to each other through the insulating links, forming a Josephson junction array (JJA) of FeSe/STO (Fig. 3b). A longer etching time induces more damage through the sidewall of the nano-holes and makes the links between superconducting areas more resistive, which increases R_N and the disorder strength (Fig. 3a).

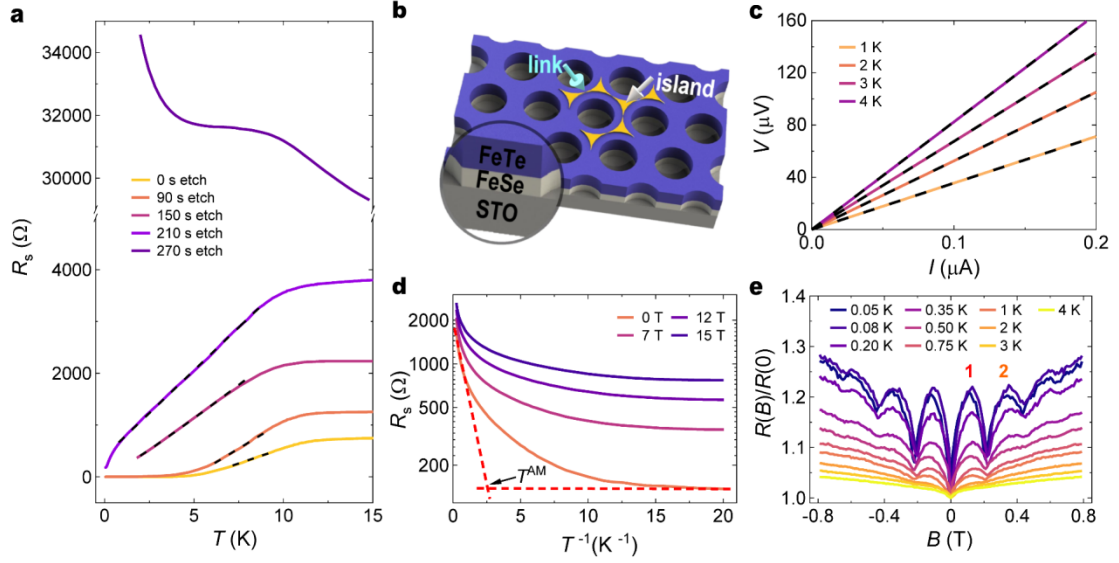


Fig. 3 T -linear resistance and anomalous metal state of nanopatterned FeSe/STO with triangular arrays of nano-holes. **a**, The $R_s(T)$ curves of FeSe films with different etching times measured with 100 nA. A shorter etching time corresponds to a smaller normal state resistance (R_N) and narrower range of linear $R_s(T)$. The linear $R_s(T)$ trend persists down to 1 K for 210 s etched film. The black dashed lines are linear fits to $R_s(T)$. **b**, Schematic for nanopatterned FeSe film on STO substrate. Superconducting areas (marked as island) are connected by insulating links. **c**, The I - V curves showing ohmic behavior within 200 nA down to 1 K for 210 s etched film. **d**, Arrhenius plots of $R_s(T)$ curves of 210 s etched sample under different magnetic fields, measured at 15 nA. **e**, Magnetoresistance from -0.8 T to 0.8 T, showing quantum oscillations. The oscillation period is around ~ 0.221 T, corresponding to one superconducting flux quantum for a unit cell pattern of 9010 nm^2 .

The superconducting transition region gets wider as R_N increases. Meanwhile, below T_c^{onset} a remarkably T -linear resistance temperature range (Fig. 3a) appears and extends with the increasing etching time from 90 s ($R_N = 1.2 \text{ k}\Omega$) to 210 s ($R_N = 3.7 \text{ k}\Omega$). The film with the etching time of 270 s shows insulating behavior at low temperatures (R_N is as high as $31.5 \text{ k}\Omega$). Note that we use a small excitation current (100 nA) within the linear regime of the I - V curve of FeSe/STO (Fig. 3c); this allows access to the intrinsic metallic transport properties of the FeSe films below T_c^{onset} . Then we performed ultralow temperature transport measurements down to 50 mK. The 0 s

and 90 s etched film exhibit a zero-resistance state at low temperatures, while 210 s etched film shows a finite resistance down to 50 mK. The resistance saturation at low temperatures for the 210 s etched film signals an anomalous metal state (Fig. 3d). The I - V measurements show linear feature within 40 nA in the ultralow temperature regime down to 50 mK (Extended Data Fig. 5). Previous studies suggest that external high frequency noise may disrupt the coherence of superconductivity at ultralow temperatures and cause artificial resistance saturation^{12,50,51}. To exclude these effects, the measurements were carried out in a dilution refrigerator cryostat with radio frequency filters. When applying a perpendicular magnetic field, the saturated resistance increases with increasing field (Fig. 3d), quite similar to the behavior of the high-temperature anomalous metal state in unpatterned FeSe films (Fig. 1c). The anomalous metal state also displays a giant positive longitudinal magnetoresistance (Extended Data Fig. 6a), which is gradually smeared out at higher temperatures. Furthermore, within ± 0.8 T the magnetoresistance oscillates with a monotonically rising background, as shown in Fig. 3e. The oscillation field period, ~ 0.221 T, is consistent with one superconducting flux quantum $\phi_0 = \frac{h}{2e}$ threading an area of one unit cell of the nanopattern (around 9010 nm^2) in the JJA (e is the electron charge). The $h/2e$ quantum oscillations persist up to 4 K (Fig. 3e), which is within the temperature regime of T -linear resistance, and thus demonstrate the bosonic nature of the observed anomalous metal and strange metal state. The resistance saturation of anomalous metal states is confirmed in more nanopatterned FeSe/STO samples, as shown in Extended Data Fig. 3.

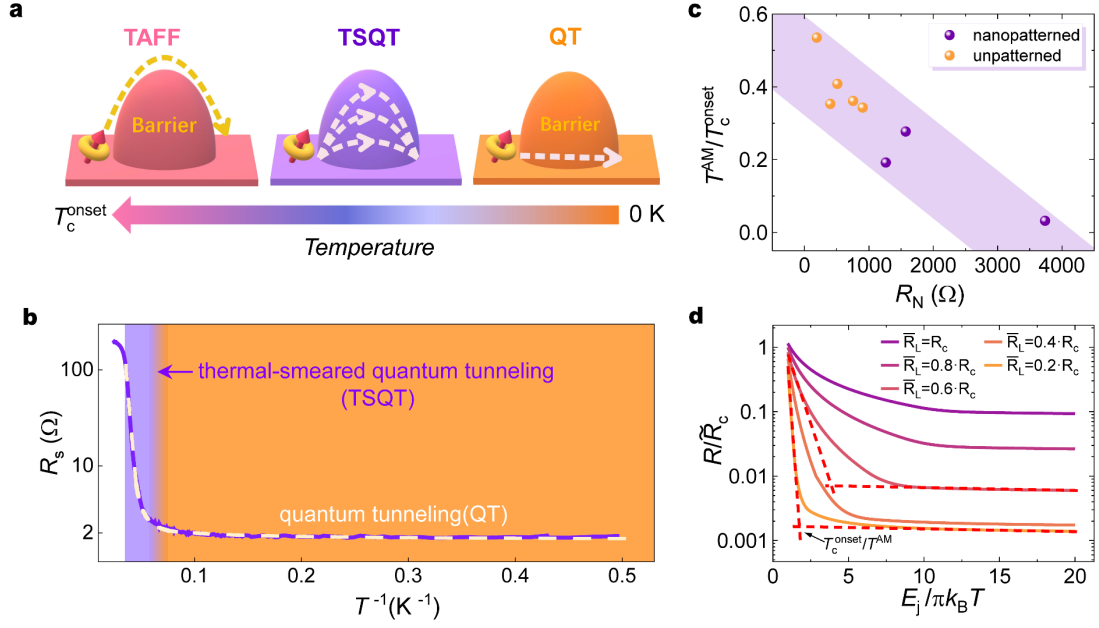


Fig. 4 The origin and evolution of anomalous metal states. **a**, Schematic diagram of vortex dynamics. Thermal activated flux flow (TAFF) is dominant in the relatively high temperature regime where the vortex motion is driven by thermal fluctuations. Quantum tunneling (QT) of vortices is dominant in the low temperature regime where the vortex motion is driven by quantum fluctuations. The thermal smeared quantum tunneling (TSQT) becomes dominant in the moderate temperature regime. **b**, The fitting result (white dashed line) of the $R_s(T)$ curve (purple line) of a high temperature anomalous metal sample (S7) by our theoretical model considering quantum tunneling of vortices in the low temperature regime (orange area) and thermal-smeared quantum tunneling in the moderate temperature regime (purple area). **c**, $T^{\text{AM}}/T_c^{\text{onset}}$ as a function of normal state resistance (R_N) at zero field for both unpatterned and nanopatterned films. $T^{\text{AM}}/T_c^{\text{onset}}$ decreases with increasing R_N . The shadow areas are guides for the eye. **d**, Quantitative simulation of the resistance-temperature behavior from vortices quantum tunneling. The panel shows $\log R/\widetilde{R}_c$ versus $E_J/\pi k_B T$ curves with different colors representing different link resistance \widetilde{R}_L . Here $E_J/\pi k_B$ is around T_c^{onset} , $R_c \equiv \frac{h}{4e^2}$, $\widetilde{R}_c \equiv \frac{h}{4e^2} \cdot \frac{E_c}{4k_B T_c^{\text{onset}}} \cdot \frac{\sqrt{\pi}}{2}$. The resistance curves have two parts, namely the thermal-smeared quantum tunneling of vortices (Eq. 1) in the moderate temperature regime and the quantum tunneling of vortices (Eq. 2) near zero temperature. $T^{\text{AM}}/T_c^{\text{onset}}$ can be calculated from the crossing point of the red dashed lines.

The electric resistance in a bosonic system are normally attributed to the classical motion of vortices at high temperatures or quantum tunneling of vortices at low temperatures⁵². The vortex motion can break the phase coherence of Cooper pairs and hence destroy the superconductivity. The well-known examples of the classical motion driven by thermal fluctuations include the free vortex motion above BKT temperature²⁸ and the thermal activated flux flow (TAFF, Fig. 4a)²⁹. When the system is under strong quantum fluctuations, the quantum tunneling events of vortices (so-called quantum creep process) instead of classical motion become predominant, which could result in the insulating state at low temperatures without dissipation. However, the ohmic dissipation, generated by the coupling between fermionic and bosonic modes⁵³, will lead to the damping in the quantum tunneling process of vortices^{32,54-56}. The dissipative quantum tunneling of vortices can give rise to the phase mode damping of Cooper pairs³², which is the key to understanding the small saturated resistance of anomalous metal states at low temperatures.

Now we analyze the behavior of anomalous metal states considering the quantum tunneling of vortices with the ohmic dissipation. In a general 2D dissipative quantum XY model considering the Josephson junction array with random link resistance R_L (random dimensionless dissipation strength γ_j), we assume the link resistance R_L satisfies a Gamma distribution $P_\Gamma(R_L)$ with the mean link resistance $\overline{R_L}$ and standard deviation σ_R . The mean link resistance $\overline{R_L}$ gives the mean value of dissipation strength $\bar{\gamma} = \frac{h}{4e^2 \overline{R_L}}$. In the moderate temperature regime, the resistance is contributed from the thermal-smeared quantum tunneling of vortices (Fig. 4a) under the influence of ohmic dissipation. Considering the dissipation strength $\bar{\gamma}$ and the phase mode damping rate in this regime^{54,57}, we derived the temperature dependence of resistance as follows

$$R_s = \frac{h}{4e^2} \cdot \frac{E_c}{4k_B T_c^{\text{onset}}} \cdot \frac{\sqrt{\pi}}{2} \frac{\Gamma(\bar{\gamma})}{\Gamma(\bar{\gamma}+1/2)} \left(\frac{\pi k_B T}{E_J} \right)^{2\bar{\gamma}-1}, \quad (1)$$

with E_c and E_J denotes the charge energy and Josephson energy, respectively (see Supplementary Note 4 for details). In the low temperature regime, the resistance is contributed from the quantum tunneling of vortices (Fig. 4a) with the link resistance $\frac{h}{(2e)^2} < R_L < \frac{2h}{(2e)^2}$ (in other words $\frac{1}{2} < \gamma < 1$). Thus, based on the phase mode damping rate in this regime³², we derived the theoretical formula for low-temperature resistance

$$R_s = \frac{C_1 h}{8\sqrt{\pi} e^2} \frac{E_c}{4k_B T_c^{\text{onset}}} \cdot \text{Exp}[T/T_0], \quad (2)$$

with the constant $C_1 = \int_{R_Q}^{2R_Q} P_\Gamma(R_L) \frac{\Gamma(\frac{\gamma}{2(1-\gamma)})}{\Gamma(\frac{1}{2(1-\gamma)})} dR_L$, $\Gamma(x)$ is the gamma function and T_0 is an intrinsic energy scale, which is related to $E_J/\pi k_B$ (see Supplementary Note 4 for details). Remarkably, the experimental $R_s(T)$ curves of eight FeSe/STO samples showing anomalous metal states can be well fitted by our theoretical model (Eqs. (1) and (2)), as shown in Extended Data Fig. 9. Specifically, the experimental $R_s(T)$ curve (the purple line) and the fitting result (white dashed line) of a typical FeSe/STO sample with high temperature anomalous metal state are shown in Fig. 4b. The low temperature regime of quantum tunneling of vortices and the moderate temperature regime of thermal-smeared quantum tunneling are marked as the orange and purple area, respectively.

The evolution of anomalous metal states with increasing normal state resistance during the quantum phase transition can be understood within our theoretical analysis. As shown in Fig. 4c, our experimental study reveals that the $T^{\text{AM}}/T_c^{\text{onset}}$ decreases with increasing normal state resistance R_N in both pristine and nanopatterned FeSe/STO. Based on our theoretical analysis, in Fig. 4d, we have plotted $\log R/\widetilde{R}_c$ versus $E_J/\pi k_B T$ curves with different colors representing different link resistance \overline{R}_L to reveal the contribution of vortex quantum tunneling with ohmic dissipation based on Eqs. (1) and (2). Here $E_J/\pi k_B$ is around T_c^{onset} and $\widetilde{R}_c \equiv \frac{h}{4e^2} \cdot \frac{E_c}{4k_B T_c^{\text{onset}}} \cdot \frac{\sqrt{\pi}}{2}$. For samples with small link resistance \overline{R}_L (large dissipation γ), the sheet resistance quickly decreases when the temperature is below T_c^{onset} , and the system quickly enters into the quantum tunneling regime with a residual resistance, suggesting a large $T^{\text{AM}}/T_c^{\text{onset}}$ value. With increasing \overline{R}_L , the $T^{\text{AM}}/T_c^{\text{onset}}$ decreases as shown by the crossing points in Fig. 4d, consistent with the experimental observations (Fig. 4c) considering that the mean value of link resistance \overline{R}_L connects to the normal state resistance R_N .

Our work reveals that the ohmic dissipation fully alters the quantum tunneling of vortices in a 2D superconducting system, which gives rise to the experimental features of anomalous metal states. Specifically, in ultrathin FeSe/STO superconductors, comparably strong dissipation leads to exceptionally high T^{AM} and $T^{\text{AM}}/T_c^{\text{onset}}$. Our investigation largely enriches the understanding of the bosonic metal states, and the

significantly high T^{AM} could bring in other experimental techniques (e.g., infrared optical conductivity), which are very difficult to be carried out at ultralow temperatures, on the studies of anomalous metal states. Moreover, the anomalous metal states in both unpatterned and nanopatterned FeSe/STO samples call for theoretical endeavors to investigate whether replica symmetry breaking⁵⁸ plays a dominant role in the ultraslow dynamics associated with quantum tunneling of vortices.

Reference

1. Phillips, P. *Advanced Solid State Physics*, (Cambridge University Press, 2012).
2. Kapitulnik, A., Kivelson, S. A. & Spivak, B. Colloquium: Anomalous metals: Failed superconductors. *Rev. Mod. Phys.* **91**, 011002 (2019).
3. Phillips, P. & Dalidovich, D. The elusive Bose metal. *Science* **302**, 243-247 (2003).
4. Breznay, N. P. & Kapitulnik, A. Particle-hole symmetry reveals failed superconductivity in the metallic phase of two-dimensional superconducting films. *Sci. Adv.* **3**, e1700612 (2017).
5. Yang, C. et al. Intermediate bosonic metallic state in the superconductor-insulator transition. *Science* **366**, 1505 (2019).
6. Jaeger, H. M., Haviland, D. B., Orr, B. G. & Goldman, A. M. Onset of superconductivity in ultrathin granular metal films. *Phys. Rev. B* **40**, 182-196 (1989).
7. Yazdani, A. & Kapitulnik, A. Superconducting-insulating transition in two-dimensional α -MoGe thin films. *Phys. Rev. Lett.* **74**, 3037-3040 (1995).
8. Qin, Y., Vicente, C. L. & Yoon, J. Magnetically induced metallic phase in superconducting tantalum films. *Phys. Rev. B* **73**, 100505 (2006).
9. Wang, Y., Tamir, I., Shahar, D. & Armitage, N. P. Absence of cyclotron resonance in the anomalous metallic phase in InO_x . *Phys. Rev. Lett.* **120**, 167002 (2018).
10. Ienaga, K., Hayashi, T., Tamoto, Y., Kaneko, S. & Okuma, S. Quantum criticality inside the anomalous metallic state of a disordered superconducting thin film. *Phys. Rev. Lett.* **125**, 257001 (2020).
11. Liu, Y. et al. Type-II Ising superconductivity and anomalous metallic state in macro-size ambient-stable ultrathin crystalline films. *Nano Lett.* **20**, 5728-5734 (2020).
12. Xing, Y. et al. Extrinsic and intrinsic anomalous metallic states in transition metal dichalcogenide Ising superconductors. *Nano Lett.* **21**, 7486-7494 (2021).
13. Garcia-Barriocanal, J. et al. Electronically driven superconductor-insulator transition in electrostatically doped $\text{La}_2\text{CuO}_{4+\delta}$ thin films. *Phys. Rev. B* **87**, 024509 (2013).
14. Saito, Y., Kasahara, Y., Ye, J., Iwasa, Y. & Nojima, T. Metallic ground state in an ion-gated two-dimensional superconductor. *Science* **350**, 409 (2015).
15. Li, L. et al. Anomalous quantum metal in a 2D crystalline superconductor with electronic phase nonuniformity. *Nano Lett.* **19**, 4126-4133 (2019).
16. Liao, M. et al. Coexistence of resistance oscillations and the anomalous metal

- phase in a lithium intercalated TiSe_2 superconductor. *Nat. Commun.* **12**, 5342 (2021).
17. Sajadi, E. et al. Gate-induced superconductivity in a monolayer topological insulator. *Science* **362**, 922-925 (2018).
 18. Eley, S., Gopalakrishnan, S., Goldbart, P. M. & Mason, N. Approaching zero-temperature metallic states in mesoscopic superconductor–normal–superconductor arrays. *Nat. Phys.* **8**, 59-62 (2012).
 19. Han, Z. et al. Collapse of superconductivity in a hybrid tin–graphene Josephson junction array. *Nat. Phys.* **10**, 380-386 (2014).
 20. Böttcher, C. G. L. et al. Superconducting, insulating and anomalous metallic regimes in a gated two-dimensional semiconductor–superconductor array. *Nat. Phys.* **14**, 1138-1144 (2018).
 21. Chen, Z. et al. Carrier density and disorder tuned superconductor-metal transition in a two-dimensional electron system. *Nat. Commun.* **9**, 4008 (2018).
 22. Chen, Z. et al. Electric field control of superconductivity at the $\text{LaAlO}_3/\text{KTaO}_3(111)$ interface. *Science* **372**, 721 (2021).
 23. Huang, D. & Hoffman, J. E. Monolayer FeSe on SrTiO_3 . *Annu. Rev. Condens. Matter Phys.* **8**, 311-336 (2017).
 24. Wang, Q.-Y. et al. Interface-induced high-temperature superconductivity in single unit-cell FeSe films on SrTiO_3 . *Chin. Phys. Lett.* **29**, 037402 (2012).
 25. Zhang, W.-H. et al. Direct observation of high-temperature superconductivity in one-unit-cell FeSe films. *Chin. Phys. Lett.* **31**, 017401 (2014).
 26. Wang, Z., Liu, C., Liu, Y. & Wang, J. High-temperature superconductivity in one-unit-cell FeSe films. *J. Condens. Matter Phys.* **29**, 153001 (2017).
 27. Blatter, G., Feigel'man, M. V., Geshkenbein, V. B., Larkin, A. I. & Vinokur, V. M. Vortices in high-temperature superconductors. *Rev. Mod. Phys.* **66**, 1125-1388 (1994).
 28. Halperin, B. I. & Nelson, D. R. Resistive transition in superconducting films. *J. Low Temp. Phys.* **36**, 599-616 (1979).
 29. Kes, P. H., Aarts, J., Berg, J. v. d., Beek, C. J. v. d. & Mydosh, J. A. Thermally assisted flux flow at small driving forces. *Supercon. Sci. Technol.* **1**, 242-248 (1989).
 30. Blatter, G., Geshkenbein, V. B. & Vinokur, V. M. Quantum collective creep. *Phys. Rev. Lett.* **66**, 3297-3300 (1991).
 31. Ao, P. & Thouless, D. J. Berry's phase and the Magnus force for a vortex line in a superconductor. *Phys. Rev. Lett.* **70**, 2158-2161 (1993).
 32. Weiss, U. *Quantum dissipative systems*, Fourth Edition (World Scientific and Singapore, 2012).
 33. Devoret, M. H., Martinis, J. M. & Clarke, J. Measurements of Macroscopic Quantum Tunneling out of the Zero-Voltage State of a Current-Biased Josephson Junction. *Phys. Rev. Lett.* **55**, 1908-1911 (1985).
 34. J, C. Quantum mechanics of a macroscopic variable: the phase difference of a josephson junction. *Science (New York, N.Y.)* **239**, 992-997 (1988).
 35. Clarke, J. & Wilhelm, F. K. Superconducting quantum bits. *Nature* **453**, 1031-1042 (2008).
 36. Wang, Q. et al. Thickness dependence of superconductivity and superconductor–insulator transition in ultrathin FeSe films on $\text{SrTiO}_3(001)$ substrate. *2D Mater.* **2**, 044012 (2015).
 37. Martin, S., Fiory, A. T., Fleming, R. M., Schneemeyer, L. F. & Waszczak, J. V. Normal-state transport properties of $\text{Bi}_{2+x}\text{Sr}_{2-y}\text{CuO}_{6\pm\delta}$ crystals. *Phys. Rev. B* **41**,

- 846-849 (1990).
38. Legros, A. et al. Universal T-linear resistivity and Planckian dissipation in overdoped cuprates. *Nat. Phys.* **15**, 142-147 (2019).
 39. Michon, B. et al. Thermodynamic signatures of quantum criticality in cuprate superconductors. *Nature* **567**, 218-222 (2019).
 40. Doiron-Leyraud, N. et al. Correlation between linear resistivity and T_c in the Bechgaard salts and the pnictide superconductor $\text{Ba}(\text{Fe}_{1-x}\text{Co}_x)_2\text{As}_2$. *Phys. Rev. B* **80**, 214531 (2009).
 41. Analytis, J. G. et al. Transport near a quantum critical point in $\text{BaFe}_2(\text{As}_{1-x}\text{P}_x)_2$. *Nat. Phys.* **10**, 194-197 (2014).
 42. Custers, J. et al. The break-up of heavy electrons at a quantum critical point. *Nature* **424**, 524-527 (2003).
 43. Bruin, J. A. N., Sakai, H., Perry, R. S. & Mackenzie, A. P. Similarity of scattering rates in metals showing T-Linear resistivity. *Science* **339**, 804-807 (2013).
 44. Cao, Y. et al. Strange metal in magic-angle graphene with near Planckian dissipation. *Phys. Rev. Lett.* **124**, 076801 (2020).
 45. Daou, R. et al. Linear temperature dependence of resistivity and change in the Fermi surface at the pseudogap critical point of a high- T_c superconductor. *Nat. Phys.* **5**, 31-34 (2009).
 46. Licciardello, S. et al. Electrical resistivity across a nematic quantum critical point. *Nature* **567**, 213-217 (2019).
 47. Shen, B. et al. Strange-metal behaviour in a pure ferromagnetic Kondo lattice. *Nature* **579**, 51-55 (2020).
 48. Gegenwart, P., Si, Q. & Steglich, F. Quantum criticality in heavy-fermion metals. *Nat. Phys.* **4**, 186-197 (2008).
 49. Jiang, X. et al. Enhancement of superconductivity linked with linear-in-temperature/field resistivity in ion-gated FeSe films. Preprint at <https://arxiv.org/abs/2103.06512> (2021).
 50. Tamir, I. et al. Sensitivity of the superconducting state in thin films. *Sci. Adv.* **5**, eaau3826 (2019).
 51. Shin, J., Park, S. & Kim, E. Effect of external electromagnetic radiation on the anomalous metallic behavior in superconducting Ta thin films. *Phys. Rev. B* **102**, 184501 (2020).
 52. Tinkham, M. *Introduction to superconductivity*, (McGraw-Hill, New York, 1996).
 53. Ambegaokar, V., Eckern, U. & Schön, G. Quantum Dynamics of Tunneling between Superconductors. *Phys. Rev. Lett.* **48**, 1745-1748 (1982).
 54. Leggett, A. J. et al. Dynamics of the dissipative two-state system. *Rev. Mod. Phys.* **59**, 1-85 (1987).
 55. Aji, V. & Varma, C. M. Theory of the quantum critical fluctuations in cuprate superconductors. *Phys. Rev. Lett.* **99**, 067003 (2007).
 56. Kapitulnik, A., Mason, N., Kivelson, S. A. & Chakravarty, S. Effects of dissipation on quantum phase transitions. *Phys. Rev. B* **63**, 125322 (2001).
 57. Chakravarty, S. & Leggett, A. J. Dynamics of the two-state system with ohmic dissipation. *Phys. Rev. Lett.* **52**, 5-8 (1984).
 58. Mézard, M., Giorgio Parisi, and Miguel Angel Virasoro. in *Spin glass theory and beyond: An Introduction to the Replica Method and Its Applications* Vol. 9 (World Scientific Publishing Company, 1987).

Methods

Film growth

Thin FeSe films (1-5 unit-cells) were epitaxially grown in an ultra-high vacuum molecular beam epitaxy (MBE) chamber. Pretreated single crystal STO (001) substrates were used for the growth²⁵. We etched the substrates with deionized water (90 °C, 45 min) and 10% HCl solution (room temperature, 45 min). Then, we annealed the substrates in a tube furnace under oxygen flow at 980 °C for 3 h. Before growth, the substrates were degassed at 600 °C for 0.5 h in MBE chamber. Through the above treatments, the STO (001) surface became atomically flat with step terrace structure and TiO₂ termination. FeSe films were then grown by co-evaporating Fe (99.995%) and Se (99.9999%) from Knudsen cells with a flux ratio of ~1:10 as the substrates were heated to 400 °C. After growth, FeSe films were gradually annealed up to 450 °C. To protect the thin FeSe films from oxidization, FeTe protection layers were grown by co-evaporating Fe (99.995%) and Te (99.9999%) with a flux ratio of ~1:4 at 270 °C. During the growth, scanning tunneling microscope was used to examine the morphology and crystal quality of the films. Our films are rectangular strips around 6 mm long and 2 mm wide, grown on substrates in 2 mm × 10 mm.

The fabrication of nano-holes array

To fabricate Josephson junction array on FeSe/STO, we etched the FeSe films by reactive ion etching (RIE) technique through anodic aluminum oxide (AAO) membrane masks. The AAO mask, with a triangular array of holes (70 nm in diameter and 100 nm in period), was transferred onto the FeSe film in acetone⁵. The etching was performed with Ar flow (20 sccm) and 200 W radio frequency power. The chamber pressure was kept around 6.0 Pa during etching. With increasing etching time, the normal state resistance increases and the film changes from superconducting state to anomalous metal and then insulating state.

Transport measurements

The six-probe configuration was used for the transport measurements, as shown in the inset of Fig. 1a. Two indium strips (I^+ and I^-) were pressed along the width of the film so that the current could homogeneously pass through the sample. The other four

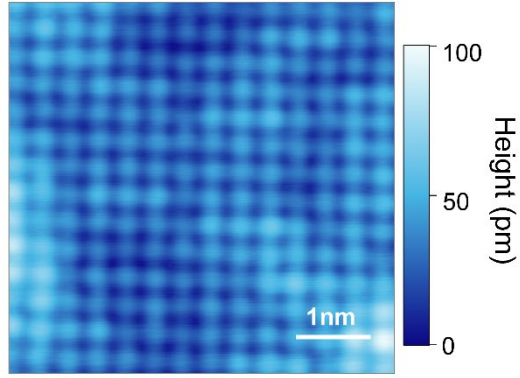
indium electrodes acted as the voltage probes. Two of them (V^+ and V^-) were used to measure the longitudinal voltage and another two electrodes (V_H) were Hall electrodes. In our measurements under parallel magnetic fields, the fields were orthogonal to the current excitations. The temperature-dependent resistance and magnetoresistance were measured in a Physical Property Measurement System (*Quantum Design*). Ultra-low temperature measurements down to 50 mK were carried out in a dilution refrigerator option with radio frequency filters (*Quantum Design*).

Data availability Data measured or analyzed during this study are available from the corresponding author on reasonable request.

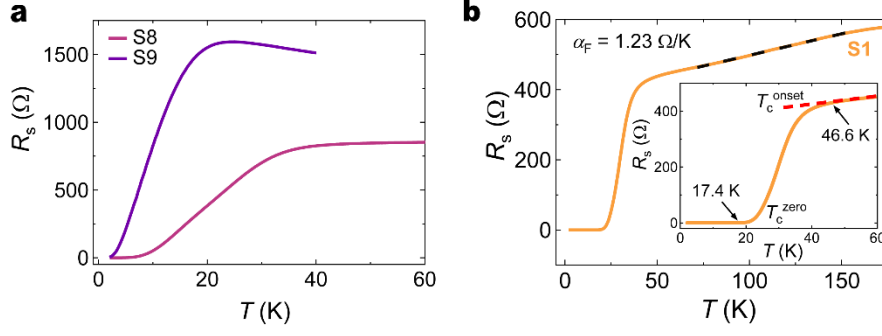
Acknowledgements We thank Xucun Ma, Guanyang He, Jie Liu, Rao Li and Yue Tang for the help in sample fabrication and characterization. We thank Zheyuan Xie for the assistance in theoretical fitting. We thank Yanzhao Liu and Ying Xing for helpful discussions. This work was financially supported by Beijing Natural Science Foundation (Z180010), the National Natural Science Foundation of China (Grant No. 11888101), the National Key Research and Development Program of China (Grant No. 2018YFA0305604, No. 2017YFA0303300), the National Natural Science Foundation of China (No. 11774008, No. 51788104, No. 12074210, No. 12174442), the Strategic Priority Research Program of Chinese Academy of Sciences (Grant No. XDB28000000), the Basic and Applied Basic Research Major Programme of Guangdong Province, China (Grant No. 2021B0301030003), Jihua Laboratory (Project No. X210141TL210), Beijing National Laboratory for Condensed Matter Physics, the Fundamental Research Funds for the Central Universities and the Research Funds of Renmin University of China.

Author contributions J.W. conceived and supervised the project. Y.N.L., Y.L., S.C.Q., H.R.J., C.C.J. and Z.H.C. analyzed the data under the guidance of J.W.. J.W., Y.N.L., Y.L., Y.S., S.C.Q. and H.R.J. performed the transport measurements. H.W.L. and X.C.X. carried out theoretical work. X.T.J., W.F.D., W.H.Z., M.H.P., L.L.W. and Q.-K.X. grew the films. Y.N.L., H.R.J. and S.C.Q. fabricated the JJA samples. Y.N.L., H.W.L., Y.L. and J.W. wrote the manuscript with the input from S.C.Q., H.R.J. and N.S.. All authors contributed the related discussions.

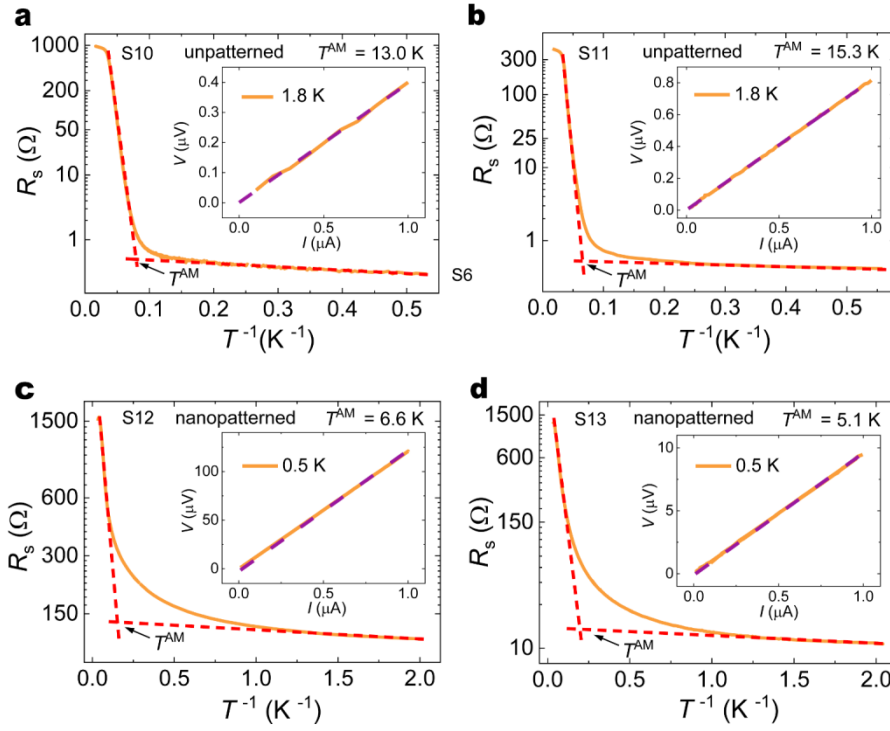
Competing interests The authors declare no competing interests.



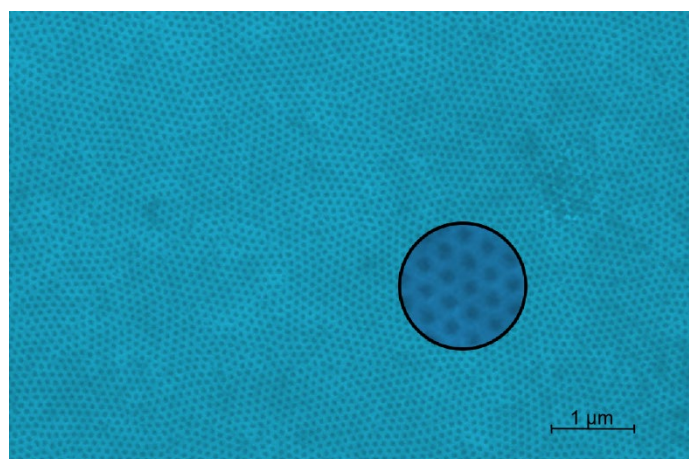
Extended Data Fig. 1| Typical STM topography of FeSe films on SrTiO₃ (001) substrates showing the lattice structure. The sample bias $V_s=80$ mV and the tunneling current $I_t=2.1$ nA. The image is 5.6×5.6 nm².



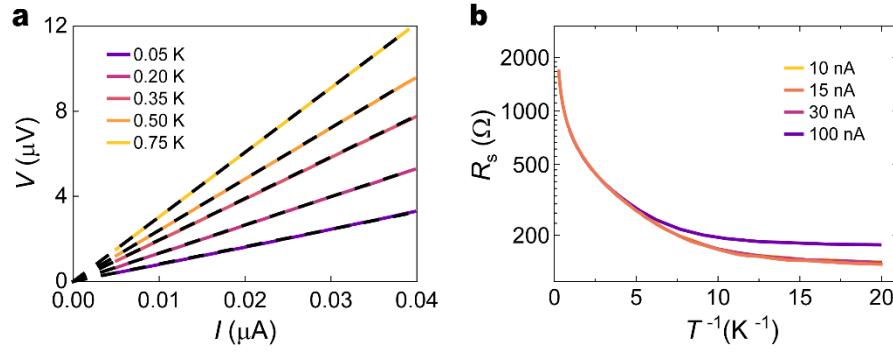
Extended Data Fig. 2 | Electric transport behavior of FeSe/SrTiO₃ at zero field. a, Temperature dependent sheet resistance $R_s(T)$ curves of FeSe/SrTiO₃ showing linear-in-temperature resistance below T_c^{onset} . The resistance either show insulating behavior or barely change above T_c^{onset} . **b,** The $R_s(T)$ curves of superconducting FeSe/SrTiO₃ (S1 in Fig. 1a). The dashed line is the linear fitting of the $R_s(T)$ curve above T_c^{onset} , yielding the slope $\alpha_F = 1.23 \text{ } \Omega/\text{K}$.



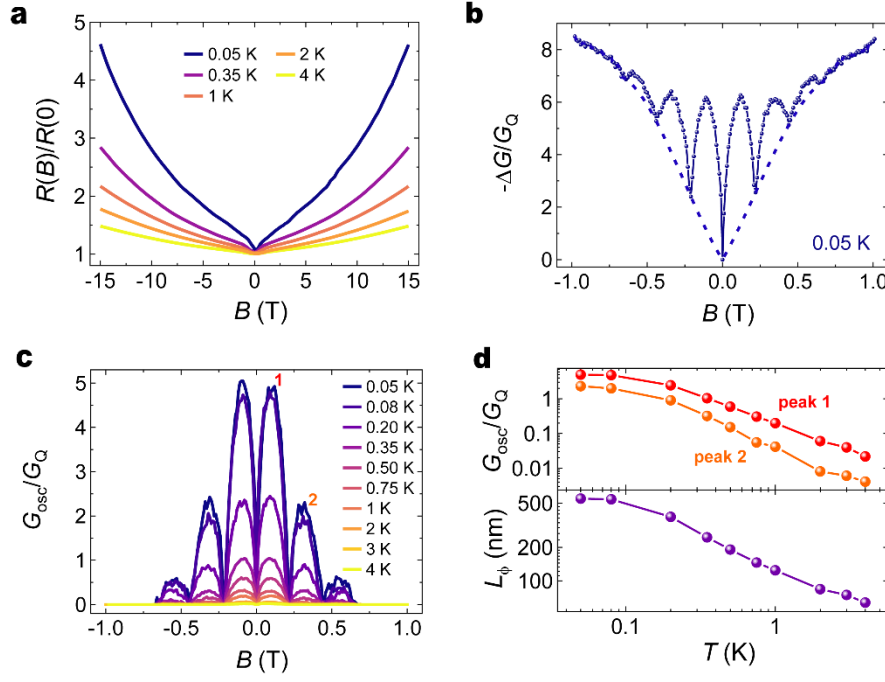
Extended Data Fig. 3 | Anomalous metal states in unpatterned (sample S10 (a), sample S11 (b)) and nanopatterned FeSe/STO (sample S12 (c), sample S13 (d)). Insets are the linear I - V curves at 0.5 K.



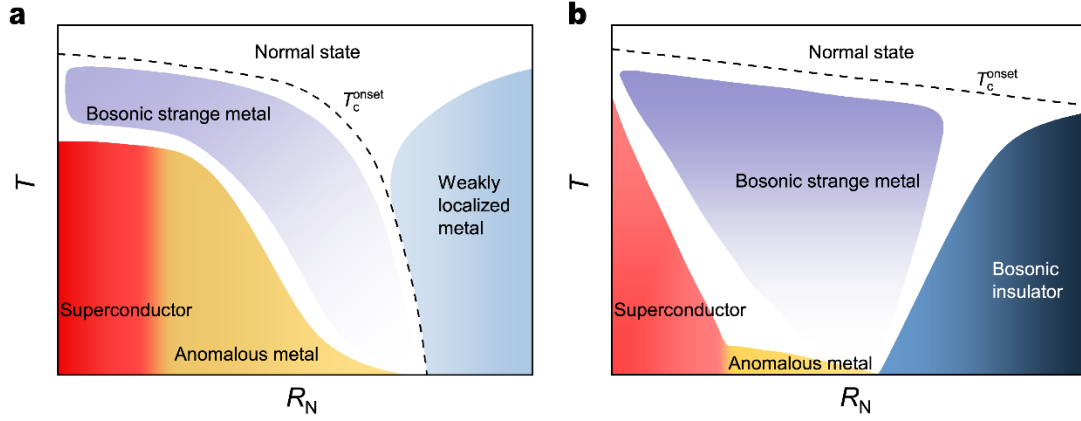
Extended Data Fig. 4 | Typical scanning electron microscope image of a nanopatterned FeSe film. The inset is the zoom-in of the nanopatterned structure.



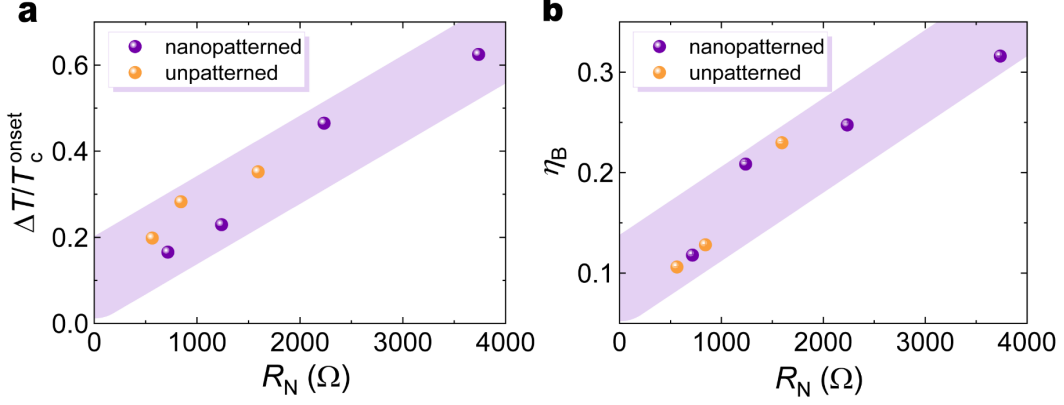
Extended Data Fig. 5 | I - V curves under different temperatures (a) and arrhenius plots of $R_s(T)$ curves under different currents (b) of 210 s etched film. The I - V curves show ohmic behavior within 40 nA down to 50 mK.



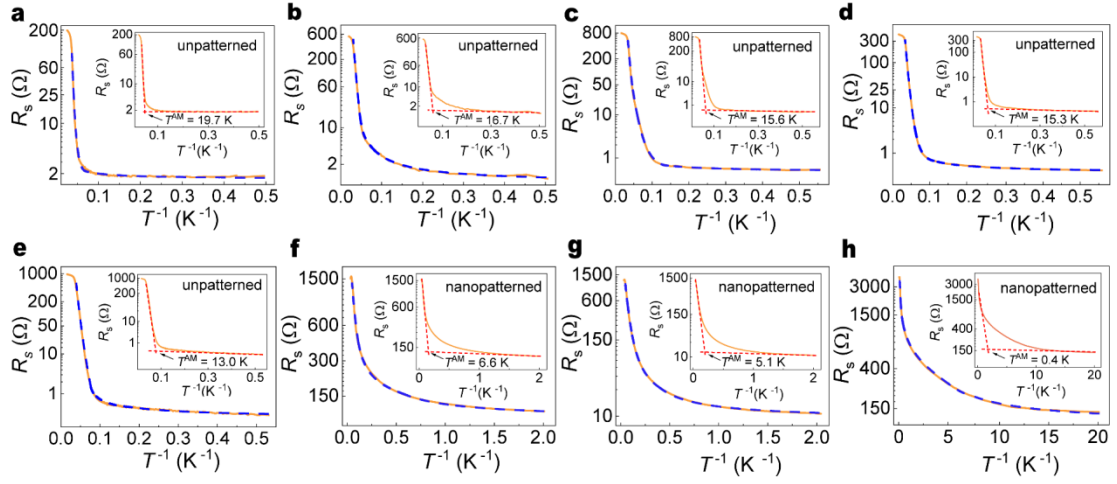
Extended Data Fig. 6 | Magneto-resistance and background subtraction of magnetoconductance oscillations of 210 s etched film showing anomalous metal state. **a**, Giant positive magnetoresistance at various temperatures from -15 T to 15 T. **b**, Negative change of magnetoconductance $-\Delta G/G_Q$ at 0.05 K. $-\Delta G = G_0 - G(B)$, where G_0 is the conductance at zero magnetic field. The dashed line is the polynomial fitting of the magnetoconductance background. **c**, Magnetoconductance oscillations at various temperatures. G_{osc} is the amplitude of conductance after subtracting the background. **d**, The amplitude of magnetoconductance oscillations G_{osc} (upper panel, the corresponding peak levels are indicated in **c**) and the phase coherence length L_ϕ (lower panel, derived from magnetoconductance oscillations of peak 2) as a function of temperature.



Extended Data Fig. 7 | The schematic phase diagrams of unpatterned FeSe/STO (a) and nanopatterned FeSe/STO samples (b). Below T_c^{onset} , superconductor, anomalous metal, and bosonic strange metal are characterized by zero resistance within the instrument resolution, residual resistance plateau, and T -linear resistance, respectively. Weakly localized metal and insulator show increasing resistance as $T \rightarrow 0$. With increasing R_N , the unpatterned FeSe/STO samples in **a** show superconductor-anomalous metal transition. The anomalous metal can persist up to 19.7 K, comparable to the zero-resistance superconducting transition temperature. With further increasing R_N , the unpatterned FeSe/STO becomes a weakly localized metal. The nanopatterned FeSe/STO samples in **b** show superconductor-anomalous metal-insulator transitions with increasing R_N . The temperature regime of anomalous metal state is relatively small, while the bosonic strange metal state occupies a large area in the phase diagram. The $\frac{h}{2e}$ quantum oscillations exist in the anomalous metal (Fig. 3e), bosonic strange metal (Fig. 3e), and insulator (Supplementary Fig. 2) states in nanopatterned FeSe/STO, indicating that Cooper pairs dominate the transport of these states.



Extended Data Fig. 8 | $\Delta T/T_c^{\text{onset}}$ (ΔT is the temperature regime of the T -linear resistance) (a), and η_B (b) as a function of normal state resistance (R_N) at zero field for unpatterned and nanopatterned FeSe/STO. Both $\Delta T/T_c^{\text{onset}}$ and η_B exhibit positive correlation with R_N . The shadow areas are guides for the eye. According to the previous works, a dimensionless coefficient $\eta_F = \frac{2e^2}{h} \cdot \alpha_F \cdot T_F$ was defined for the slope α_F of fermionic strange metal, where T_F is the Fermi temperature and η_F is around 0.2-1.6^{38,44}. Here, in our system, the T -linear resistance manifests below T_c^{onset} , allowing us to define an effective coefficient $\eta_B = \frac{2e^2}{h} \cdot \alpha_B \cdot T_c^{\text{onset}}$ by analogy, where T_c^{onset} represents the characteristic energy scale for Cooper pairs. As shown in Fig. 4c, the typical value of η_B is around 0.1-0.3 for FeSe/STO samples showing T -linear resistance.



Extended Data Fig. 9 | Fitting results with Eq. (SE15) of anomalous metal states in unpatterned and nanopatterned FeSe/STO. The blue dashed lines are the fitting curves with our theoretical model, and the orange lines are the experimental $R_s(T)$ curves. **a**, Sample S7. **b**, Sample S2. **c**, Sample S6. **d-g**, Samples S10, S11, S12 and S13. **h**, 210 s etched film as shown in Fig. 3a. The fitting parameters are shown in Extended Data Table 1.

Extended Data Table 1 | Fitting parameters of $R_s(T)$ curves with our theoretical model for anomalous metal states. The fitting curves are shown in Extended Data Fig. 9. Here, T^* is chosen to be near T_c^{onset} .

	$R_s = A \cdot \left(\frac{T}{T^*}\right)^\gamma, T^* = 35 \text{ K}$		$R_s = B \cdot \text{Exp}\left(\frac{T}{T_0}\right)$	
Sample #	$A(\Omega)$	γ	$B(\Omega)$	$T_0(\text{K})$
S2	774.9	7.7	0.9	8.6
S6	2372.6	8.3	0.5	21.8
S7	1544.0	11.8	1.7	60.2
S10	1197.3	8.0	0.4	15.2
S11	9799.5	8.9	0.3	9.4
S12	3020.3	1.4	97.1	3.7
S13	2659.9	1.8	9.1	2.3
210 s etch	10715.3	0.9	103.3	0.2

Supplementary Information for
Bosonic metal states in crystalline iron-based superconductors at the two-
dimensional limit

Yanan Li^{1,6#}, Haiwen Liu^{2#}, Shichao Qi¹, Haoran Ji¹, Xiaotong Jiao^{3,5}, Wenfeng Dong³,
Yi Sun¹, Wenhao Zhang^{3,8}, Chengcheng Ji¹, Zihan Cui⁴, Minghu Pan⁵, Nitin Samarth⁶,
Lili Wang³, X.C. Xie^{1,10,11}, Qi-Kun Xue^{3,11,12}, Yi Liu^{4,7*}, and Jian Wang^{1,9,10,11*}

¹*International Center for Quantum Materials, School of Physics, Peking University, Beijing 100871, China*

²*Center for Advanced Quantum Studies, Department of Physics, Beijing Normal University, Beijing 100875, China*

³*State Key Laboratory of Low-Dimensional Quantum Physics, Department of Physics, Tsinghua University, Beijing 100084, China*

⁴*Department of Physics, Renmin University of China, Beijing 100872, China*

⁵*School of Physics and Information Technology, Shaanxi Normal University, Xi'an 710119, China*

⁶*Department of Physics, The Pennsylvania State University, University Park, Pennsylvania 16802, USA*

⁷*Beijing Key Laboratory of Opto-electronic Functional Materials & Micro-Nano Devices, Renmin University of China, Beijing 100872, China*

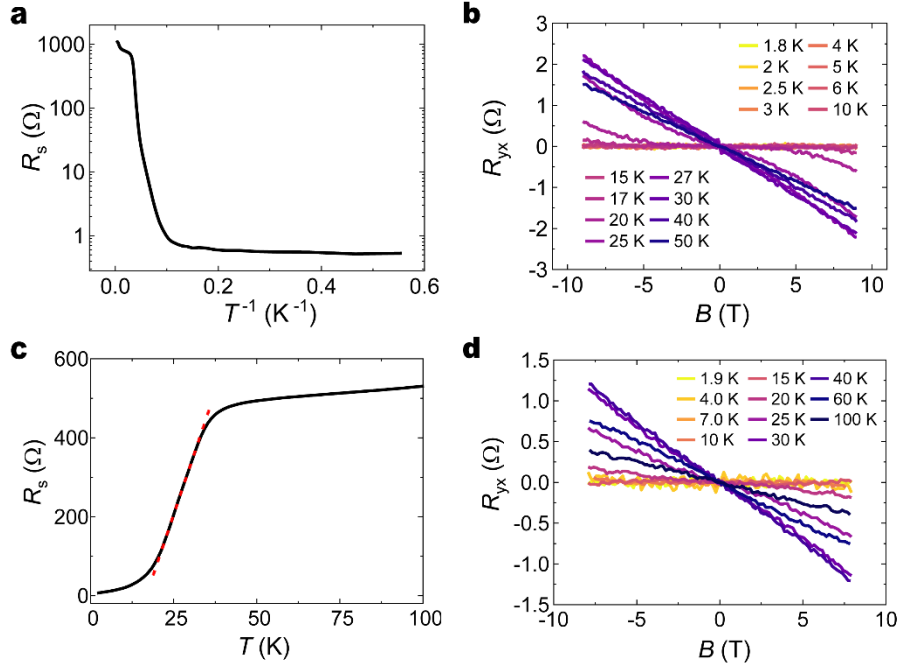
⁸*School of Physics and Wuhan National High Magnetic Field Center, Huazhong University of Science and Technology, Wuhan 430074, China*

⁹*Collaborative Innovation Center of Quantum Matter, Beijing 100871, China*

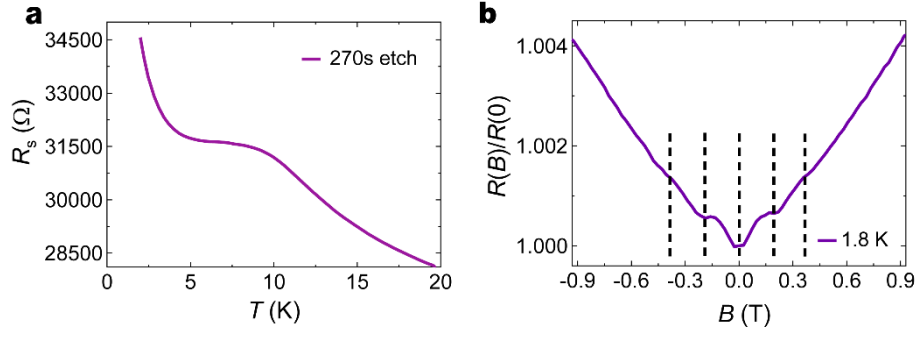
¹⁰*CAS Center for Excellence in Topological Quantum Computation, University of Chinese Academy of Sciences, Beijing 100190, China*

¹¹*Beijing Academy of Quantum Information Sciences, Beijing 100193, China*

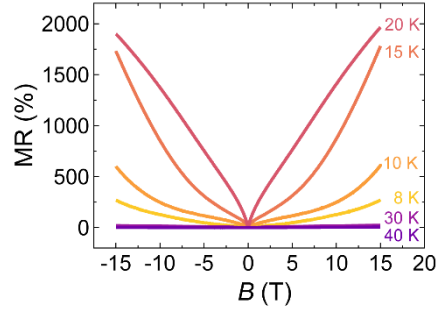
¹²*Southern University of Science and Technology, Shenzhen 518055, China*



Supplementary Figure 1 | $R_s(T)$ curves (a, c) and Hall resistance under perpendicular magnetic fields (b, d) of FeSe/SrTiO₃. a and b are the experimental data for sample S6. c and d are the data for sample S3. The Hall resistance decreases to zero within the measurement resolution below 20 K.



Supplementary Figure 2 | Insulating state of nanopatterned FeSe/SrTiO₃ (270 s etched film). **a**, $R_s(T)$ curve of 270 s etched FeSe film, showing a bosonic insulating state. In the framework of superconductor-insulator transitions, normally the bosonic insulator refers to the samples with resistance larger than the sheet resistance of quantum critical point, which is the quantum resistance of Cooper-pairs ($h/(2e)^2 \approx 6.45 \text{ k}\Omega$)¹. The sheet resistance of 270 s etched film is around 34.6 k Ω at 1.8 K, which is much larger than 6.45 k Ω . **b**, Magnetoresistance of 270 s etched FeSe film at 1.8 K. Magnetoresistance oscillations with period $\sim 0.215 \text{ T}$ are observed, corresponding to one superconducting flux quantum per unit cell of the nanopattern, which indicates the bosonic nature of the insulating state.



Supplementary Figure 3 | Magnetoresistance comparison between the high-temperature anomalous metal state and normal state of FeSe/STO (S7 in Fig. 1c).

The magnetoresistance ($MR=(R(B)-R(0))/R(0)\times 100\%$) is 270%-1900% below T^{AM} (20 K) at 15 T. Above T_c^{onset} , the magnetoresistance is only 3.5% at 40 K and 15 T.

Supplementary Note 1. Quantum oscillations in nanopatterned FeSe/STO

The $h/2e$ oscillations are observed in both the anomalous metal state and the insulating state (Extended Data Fig. 6 and Supplementary Fig. 2), which demonstrates that Cooper pairs dominate the transport in these states. The temperature dependence of the oscillation amplitude is extracted as $G_{\text{osc}} = \left| G\left(\frac{B_0}{2}\right) - G_0 \right|$ after subtracting the background, where G_0 and $G\left(\frac{B_0}{2}\right)$ are the conductance of peak and dip of each oscillation, as shown in Extended Data Fig. 6d. The phase coherence length (L_ϕ) of Cooper pairs is estimated by $G_{\text{osc}} = \frac{4e^2}{h} \left(\frac{L_\phi}{\pi r}\right)^{1.5} \exp\left(-\frac{\pi r L_\phi}{L_\phi}\right)^2$. G_Q is the quantum conductance for Cooper pairs, $\frac{4e^2}{h}$. G_{osc} and L_ϕ saturate at low temperatures (Extended Data Fig. 6d), reminiscent of the anomalous metal state in nanopatterned $\text{YBa}_2\text{Cu}_3\text{O}_{7-x}$ films².

Supplementary Note 2. Exclusion of classical percolation model for anomalous metal state

The anomalous metal state in FeSe/STO interface superconductor exhibits various interesting phenomena, including resistance saturation at low temperatures, zero Hall resistance, large magnetoresistance and linear I - V curves. These features cannot be explained by the classical percolation model³, where the local superconducting regions are embedded in the normal state. In such case, although the combination of the zero-resistance superconducting and normal state regions may satisfy the requirement of linear I - V curve, large magnetoresistance is not expected (the magnetoresistance is very small for the normal state as presented in Supplementary Fig. 3 and vice versa, which are inconsistent with our observations. In addition, the classical percolation model, in which the finite resistance is contributed by the normal state, is contradict to the observation of zero Hall resistance⁴. Therefore, the above discussion demonstrates that the classical percolation model can be excluded.

Supplementary Note 3. Discussion about the influence from FeTe capping layer on the bosonic metal states.

In pristine FeTe/STO, the sheet resistance is above 3700 ohms below 20 K⁵. In this work, the resistance of anomalous metal states saturates to a small finite value (around

0.1-10 Ω) in pristine FeSe/STO, around 10-100 ohms in nanopatterned FeSe/STO at low temperatures (Extended Data Fig. 9). The saturated resistance value of anomalous metal state in both pristine and nanopatterned FeSe/STO is far smaller than the resistance of pristine FeTe film at low temperatures. Therefore, the influence of FeTe capping layer on the anomalous metal behavior can be negligible.

As for the possible influence of FeTe capping layer on the strange metal phase (if exist), control experiments have been performed to study the effect of FeTe layer on nanopatterned FeSe/STO. The FeTe/STO system is grown and then etched for 270 s with the same procedure as FeSe/STO samples. The nanopatterned FeTe/STO system becomes very insulating with the sheet resistance as large as $2 \times 10^7 \Omega$ at 300 K, several orders of magnitude larger than that of the 270 s etched FeSe/STO. Therefore, the resistance of nanopatterned FeTe capping layer should be much larger than that of the corresponding FeSe/STO samples with the same etching time. Thus, the transport properties in the nanopatterned FeSe/STO cannot be attributed to the FeTe capping layer.

Furthermore, in our current theoretical consideration, the coupling between the bosonic modes and the fermionic modes contributes to the ohmic dissipation⁶ in the 2D dissipative quantum XY model with the dissipation coefficient $\gamma = \frac{h}{4e^2 R_L}$ (here the resistance R_L collects the contribution of the fermionic modes). Thus, the influence of FeTe capping layer (if exist) as the parallel fermionic channels has been considered in the dissipation coefficient γ .

Supplementary Note 4. Discussion on the origin of bosonic anomalous metal and bosonic strange metal

The electric resistance in a pure bosonic system can be attributed to the classical motion or quantum tunneling of vortices⁷. The well-known examples of classical motion include **case A** the free vortices motion above BKT temperature⁸, and **case B** the thermal activated flux flow under magnetic field⁹. The above-mentioned case A and case B has one respective difference that in **case A** the resistance is mainly dominated by the prefoliation of vortices density while for **case B** the resistance is mainly determined by the diffusion coefficient. Without dissipation, when the temperature

decreases to approaching zero, the quantum tunneling events of vortices become predominant (resulting in an insulator) or reduce to zero (resulting in a superconductor). This novel type of superconductor-insulator transition (SIT) can be attributed to competition between the charging energy E_c and Josephson energy E_J , and this SIT usually possess the characteristic of duality between charge and vortices with the critical quantum resistance $R_c = \frac{h}{4e^2}$ ^{10,11}. On the other hand, the coupling between fermionic modes and bosonic modes leads to the ohmic dissipation¹², and the ohmic dissipation effect will change the microscopic dynamics of vortices¹³⁻¹⁵, which further gives rise to observable consequence in experiments¹⁶⁻¹⁸. In the following, we demonstrate that the ohmic dissipation with moderate strength fully changes the dynamics of vortices tunneling beyond the aforementioned two cases and gives rise to the experimental features of anomalous metal and bosonic strange metal.

The 2D dissipative quantum XY model provides a microscopic basis for the analysis of vortices dynamics^{6,15,19} with the action:

$$S = \sum_j \int d\tau \left\{ \frac{|\dot{\theta}_j|^2}{2E_{c,j}} - \sum_{\langle i,j \rangle} E_J \cos[\theta_i - \theta_k] \right\} + \sum_j \frac{\gamma_j}{4\pi} \int d\tau_1 d\tau_2 \left| \frac{e^{i\theta_j(\tau_1)} - e^{i\theta_j(\tau_2)}}{\tau_1 - \tau_2} \right|^2. \quad (\text{SE1})$$

Here, $E_{c,j}$ denotes the charge energy at site j , E_J denotes the local Josephson energy and $\gamma_j = \frac{h}{4e^2 R_L}$ denotes the dimensionless dissipation strength determined by the link resistance R_L . The parameters E_c , E_J and γ_j are in general random numbers.

(A) The damping of phase in a uniform system

Previously, in systems with homogenous γ , it is shown that the dissipation can drive a quantum phase transition between superconductor and metal¹⁶. In order to combine this zero-temperature phase diagram with quantum dynamics of vortices, we firstly focus on the action at one single Josephson junction, namely the shunted Josephson junction model^{16,20}:

$$S = \int d\tau \left\{ \frac{|\dot{\theta}|^2}{2E_c} - E_J \cos[\theta] \right\} + \frac{\gamma}{4\pi} \int d\tau_1 d\tau_2 \left| \frac{\theta(\tau_1) - \theta(\tau_2)}{\tau_1 - \tau_2} \right|^2. \quad (\text{SE2})$$

This action can be viewed as dissipative quantum diffusion phase in the potential $E_J \cos[\theta]$. When we discuss the dissipation driven SIT, we consider the case $E_c \ll E_J$ and the γ is of order one. Thus, for 2D dissipative quantum XY model, the two

representative energy scale is the high frequency cutoff $\omega_c = \frac{E_J}{\hbar}$ and the low-energy plasma frequency $\omega_p = \frac{\sqrt{E_c \cdot E_J}}{\hbar}$ 21. The dynamics of the phase θ can be mapping to the dynamics of spin population $n_s(t)$ in the spin-boson model $\langle n_s(t)n_s(0) \rangle \propto e^{\frac{-t}{\tau_s}}$ with the damping rate in the moderate temperature regime obeying the relation²²:

$$\frac{1}{\tau_s} = \frac{\omega_p^2}{\omega_c} \frac{\sqrt{\pi}}{2} \frac{\Gamma(\gamma)}{\Gamma(\gamma+1/2)} \left(\frac{\pi k_B T}{\hbar \omega_c} \right)^{2\gamma-1}. \quad (\text{SE3})$$

One can directly find around the critical link resistance $R_L = \frac{\hbar}{4e^2}$ with $\gamma = 1$, the damping rate has a very simple form:

$$\frac{1}{\tau_s} = \frac{E_c}{E_J} \frac{\pi k_B T}{\hbar}. \quad (\text{SE4})$$

We need to mention that around the critical link resistance the damping time generally satisfies the relation $\frac{\hbar}{\tau_s} = O(1) \cdot k_B T$. Considering the above damping rate formula with the resistance in the Drude form, one can obtain the sheet resistance:

$$R_s = \frac{m^*}{n_s (2e)^2} \cdot \frac{1}{\tau_s}. \quad (\text{SE5})$$

And considering the relation between cooper pair mass m^* and superfluid density n_s and the 2D superconducting (onset) temperature T_c^{onset} with relation $\frac{\pi \hbar^2 n_s}{2m^*} = k_B T_c^{\text{onset}}$ 23,24, the resistance reads:

$$R_s = \frac{\hbar \hbar}{4k_B T_c^{\text{onset}} (2e)^2} \cdot \frac{1}{\tau_s}. \quad (\text{SE6})$$

Thus, the general resistance can be obtained $R_s \propto T^{2\gamma-1}$. Around the critical link resistance with $\gamma = 1$, the resistance has a linear R - T form:

$$R_s = \frac{\pi E_c}{4E_J} \frac{\hbar}{(2e)^2} \cdot \frac{T}{T_c^{\text{onset}}}, \quad (\text{SE7})$$

with the slope of linear-in-temperature resistance $dR_s/dT = \frac{\pi E_c}{4E_J} \frac{\hbar}{(2e)^2 T_c^{\text{onset}}}$. The optimal slope of linear R - T is approaching $\frac{\hbar}{(2e)^2 T_c^{\text{onset}}}$, but the general case of R - T is smaller due to the factor $\frac{\pi E_c}{4E_J}$. Based on the linear R - T form $R_s = \frac{\pi E_c}{4E_J} \frac{\hbar}{(2e)^2} \cdot \frac{T}{T_c^{\text{onset}}}$ around $\gamma = 1$, the slope of the system with similar T_c^{onset} is predominantly determined by $\frac{E_c}{E_J}$, and mainly represents the damping rate of phase difference θ at the Josephson junction with the form $\frac{1}{\tau_s} = \frac{E_c}{E_J} \frac{\pi k_B T}{\hbar}$ for system with given T_c^{onset} . In the samples with smaller R_N , the superconducting islands are larger with relatively smaller E_c and smaller $\frac{E_c}{E_J}$,

thus the slope positively correlates with R_N .

The Landau overdamped ($z=2$) mechanism on the pairing field also provides a phenomenological explanation for the marginal Fermi liquid²⁵⁻²⁷. Here, we mainly focus on the contribution from the microscopic vortices dynamics on the measured resistance in a 2D system to understand both the bosonic anomalous metal and strange metal states, thus we start from the 2D dissipative XY model as shown in Eq. (SE1).

(B) The diffusion of vortices in a uniform system

The damping rate of the phase can also link with the diffusion coefficient of vortices. In the following, we will show that both the spatial-domain diffusion process of vortices (shown in Eq. (SE9)) and the time-domain damping process of phase (shown in Eq. (SE3)) give the same result to illustrate the resistance of 2D dissipative superconductors. Generally, the resistance in a 2D superconductor thin film originates from the mobile vortices with the novel relation⁸:

$$R_s = \frac{h^2}{4e^2} n_v \mu_v, \text{ (SE8)}$$

here n_v denotes the density of vortices and the mobility of vortices satisfies the relation $\mu_v = \frac{\tau_v}{m_v}$ with τ_v and m_v denotes the mean free time and mass of vortices, respectively. Considering the Drude form of resistance in Eq. (SE5), one can rewrite Eq.(SE8) in the following convenient form:

$$n_s \mu_s n_v \mu_v \approx h^2. \text{ (SE9)}$$

In the following, we discuss this relation in the moderate temperature regime and in the zero-temperature regime in the 2D dissipative quantum XY model. The diffusion of vortices in this system can be viewed as the quantum Brownian motion vortices in corrugated potential with dissipation, and the mobility of the systems in the moderate temperature regime reads²⁸:

$$\mu_v = \mu_{v,0} \cdot \frac{\sqrt{\pi}}{2} \frac{\Gamma(\gamma)}{\Gamma(\gamma+1/2)} \left(\frac{\pi k_B T}{\hbar \omega_c} \right)^{2\gamma-1}, \text{ (SE10)}$$

here $\mu_{v,0} \approx A \frac{d^2}{h}$ denotes the bare vortices mobility with the inter-vortices distance d and a prefactor A . One can easily find that the mobility of vortices in Eq. (SE10) decreases with decreasing temperature for $\gamma > \frac{1}{2}$ and acts oppositely for $\gamma < \frac{1}{2}$. This behavior indicates a quantum phase transition around $\gamma = \frac{1}{2}$, which is consistent with

the previous prediction in 2D dissipative superconductors with $E_c \ll E_J$ ¹⁶. We define the characteristic time of cooper pair $\frac{1}{\tau_{s,0}} = \frac{\omega_p^2}{\omega_c} = \frac{E_c}{\hbar}$, and $\mu_{s,0} = \frac{\tau_{s,0}}{m^*}$. Thus, the bare parameters with relation $n_s \mu_{s,0} n_v \mu_{v,0} \approx \hbar^2$ gives a constraint for the prefactor $A = \frac{E_c}{4k_B T_c^{\text{onset}}}$. Then, with the moderate temperature vortices mobility relation (SE10) and the moderate temperature damping rate of phase in the (SE3), one can check equation (SE9) satisfies for the general case.

We want to elaborate on the importance of Eq. (SE9) and briefly mention why this relation can be generalized beyond the well-known examples of resistance in superconductors including the free vortices motion in BKT transition and the thermal activated flux flow. Previously, without dissipation, the quantum phase transition of SIT driven by the competition between charge energy and Josephson energy is well established^{10,11}. Meanwhile a strong dissipation with $\gamma \gg 1$ and $E_c \ll E_J$ will stabilize the superconducting phase; no quantum phase transition but thermal BKT transition occurs. Thus, under influence of dissipation, interesting quantum dynamics of vortices emerges in the moderate strength case with $\gamma \sim O(1)$. The spatial-domain diffusion analysis of vortices applies both for the uniform systems and disordered systems.

(C) The resistance in the zero-temperature limit and the influence of randomness in γ on the resistance

The damping rate and diffusion coefficient in Eq. (SE3) and (SE10) break down in the zero-temperature limit^{13,14,22}. In the zero-temperature limit, the renormalized mobility of vortices manifest three respective features¹⁴: for $\gamma > 1$ the vortices localizes with $\mu_v = 0$, for $\gamma < \frac{1}{2}$ the dynamics of vortices cannot be viewed as a diffusion process, and for $\frac{1}{2} < \gamma < 1$, the mobility reads:

$$\mu_v = \frac{c}{2\sqrt{\pi}} \cdot \mu_{v,0} \cdot \frac{\Gamma\left(\frac{\gamma}{2(1-\gamma)}\right)}{\Gamma\left(\frac{1}{2(1-\gamma)}\right)}. \quad (\text{SE11})$$

The mobility as a function of γ in Eq. (SE11) smoothly connects with the zero mobility for $\gamma > 1$. We also note another recent theoretical prediction of nonzero mobility within the regime $\frac{1}{2} < \gamma < 1$ with different functional form of γ ²⁹. This nonzero mobility of vortices will give rise to a resistance in the low-temperature regime:

$$R_s = \frac{h^2}{8\sqrt{\pi}e^2} n_v C \cdot \mu_{v,0} \cdot \frac{\Gamma\left(\frac{\gamma}{2(1-\gamma)}\right)}{\Gamma\left(\frac{1}{2(1-\gamma)}\right)}, \quad (\text{SE12})$$

here C is a constant of order one, and we choose $C \approx 1$ for simplicity in the following. The low-temperature quantum tunneling of vortices can give rise to the anomalous quantum metal in experiments.

We next discuss on the effect of random link resistance R_L and thus random γ_j . We assume the link resistance R_L satisfies a Gamma distribution $P_\Gamma(R_L)$ with the mean link resistance $\overline{R_L}$ and standard deviation σ_R . The mean link resistance $\overline{R_L}$ gives the mean value of dimensionless dissipation parameter $\bar{\gamma} = \frac{h}{4e^2 \overline{R_L}}$ (the random dissipation parameter $\gamma = \frac{h}{4e^2 R_L}$), and the moderate temperature resistance can be approximated by the simple version contributed from the thermal-smeared quantum tunneling of vortices:

$$R_s = \frac{h}{4e^2} \cdot \frac{E_c}{4k_B T_c^{\text{onset}}} \cdot \frac{\sqrt{\pi}}{2} \frac{\Gamma(\bar{\gamma})}{\Gamma(\bar{\gamma}+1/2)} \left(\frac{\pi k_B T}{E_J} \right)^{2\bar{\gamma}-1}. \quad (\text{SE13})$$

Here we utilize the approximation $n_v \mu_{v,0} \approx A n_v \frac{d^2}{h} \approx \frac{A}{h} \approx \frac{E_c}{4k_B T_c^{\text{onset}}} \cdot \frac{1}{h}$, with E_c denoting the charging energy and T_c^{onset} denoting the onset superconducting temperature. The low temperature resistance is contributed by the link resistance $R_Q < R_L < 2R_Q$ (in other words $\frac{1}{2} < \gamma < 1$). Thus, the resistance in the low temperature regime reads:

$$R_s = \frac{C_1 h}{8\sqrt{\pi}e^2} \frac{E_c}{4k_B T_c^{\text{onset}}} \cdot \text{Exp}[T/T_0], \quad (\text{SE14})$$

with the constant $C_1 = \int_{R_Q}^{2R_Q} P_\Gamma(R_L) \frac{\Gamma\left(\frac{\gamma}{2(1-\gamma)}\right)}{\Gamma\left(\frac{1}{2(1-\gamma)}\right)} dR_L$, and T_0 is an intrinsic energy scale,

which is related to $E_J/\pi k_B$. Thus, the residual resistance is predominated by the distribution of link resistance, and the total dimensionless resistance can be written in a simplified form:

$$\frac{R_s}{\frac{h\sqrt{\pi}}{8e^2} \frac{E_c}{4k_B T_c^{\text{onset}}}} = \begin{cases} \frac{\Gamma(\bar{\gamma})}{\Gamma(\bar{\gamma}+1/2)} \left(\frac{\pi k_B T}{E_J} \right)^{2\bar{\gamma}-1}, & \text{moderate} - T \text{ regime} \\ \frac{C_1}{\pi} \text{Exp}[T/T_0], & \text{low} - T \text{ regime} \end{cases}. \quad (\text{SE15})$$

Thus, given the distribution of link resistance, one can briefly draw the resistance versus temperature based on Eq. (SE15). And the crossing point of these two curves separates the moderate- T resistance behavior and the low- T bosonic anomalous metal feature. We

give out the specific case for the crystalline samples and the nanopatterned samples.

For the crystalline samples, the mean value of link resistance $\overline{R_L}$ is smaller than R_Q thus $\bar{\gamma} > 1$, and meanwhile the link is much randomized with a large σ_R . Thus, the moderate temperature resistance-temperature relation becomes superlinear, and the resistance quickly diminishes to approaching zero under T_c^{onset} . For samples with smaller $\overline{R_L}$, the resistance decreases quickly. Moreover, for samples with smaller $\overline{R_L}$, the zero-temperature mobile vortices frequency $P(R_Q < R_L < 2R_Q)$ is also smaller. Thus, when decreasing the normal state resistance in crystalline samples, one can obtain an enlarged bosonic anomalous metal temperature regime, as shown in Fig. 4a and Extended Data Fig. 8.

For the nanopatterned samples, the mean value of link resistance $\overline{R_L}$ can be tuned to approaching the optimal value R_Q thus $\bar{\gamma} = 1$, and meanwhile the link is relatively uniform with a small σ_R . Thus, the moderate temperature resistance-temperature relation become liner, namely the bosonic strange metal feature. Moreover, due to the small value of standard deviation σ_R , the link resistance locates near R_Q and the low-temperature mobility of vortices becomes very small as shown in Eq. (SE15). Thus, in the nanopatterned samples with optimal link resistance $\overline{R_L} \approx R_Q$, the bosonic strange metal feature becomes remarkable while the bosonic anomalous metal feature is not obvious.

Based on Eq. (SE15), the experimental $R_s(T)$ curves of anomalous metal states are fitted by the above theoretical model (Extended Data Fig. 9). At low temperatures, the $R_s(T)$ curves are fitted by a simplified formula $R_s = B \cdot \text{Exp}(\frac{T}{T_0})$, which accounts for the quantum tunneling behavior of vortices. At moderate temperatures, the $R_s(T)$ curves are fitted by a simplified formula $R_s = A \cdot (\frac{T}{T^*})^\gamma$, which accounts for the thermal-smeared quantum tunneling behavior of vortices. Between these two temperature ranges, the fitting curves are connected by a smooth Bezier function. The fitting parameters are listed in Supplementary Table 1.

1. Goldman, A. M. Superconductor-insulator transitions. *Int. J. Mod. Phys* **24**,

- 4081-4101 (2010).
2. Yang, C. et al. Intermediate bosonic metallic state in the superconductor-insulator transition. *Science* **366**, 1505-1509 (2019).
3. Kapitulnik, A., Kivelson, S. A. & Spivak, B. Colloquium: Anomalous metals: Failed superconductors. *Rev. Mod. Phys.* **91**, 011002 (2019).
4. Breznay, N. P. & Kapitulnik, A. Particle-hole symmetry reveals failed superconductivity in the metallic phase of two-dimensional superconducting films. *Sci. Adv.* **3**, e1700612 (2017).
5. Zhang, W.-H. et al. Direct Observation of High-Temperature Superconductivity in One-Unit-Cell FeSe Films. *Chin. Phys. Lett.* **31**, 017401 (2014).
6. Eckern, U., Schön, G. & Ambegaokar, V. Quantum dynamics of a superconducting tunnel junction. *Phys. Rev. B* **30**, 6419-6431 (1984).
7. Tinkham, M. *Introduction to Superconductivity*. (McGraw-Hill, New York, (1996)).
8. Halperin, B. I. & Nelson, D. R. Resistive transition in superconducting films. *J. Low Temp. Phys.* **36**, 599-616 (1979).
9. Kes, P. H., Aarts, J., Berg, J. v. d., Beek, C. J. v. d. & Mydosh, J. A. Thermally assisted flux flow at small driving forces. *Supercond. Sci. Technol.* **1**, 242-248 (1989).
10. Fisher, M. P. A., Weichman, P. B., Grinstein, G. & Fisher, D. S. Boson localization and the superfluid-insulator transition. *Phys. Rev. B* **40**, 546-570 (1989).
11. Fisher, M. P. A., Grinstein, G. & Girvin, S. M. Presence of quantum diffusion in two dimensions: Universal resistance at the superconductor-insulator transition. *Phys. Rev. Lett.* **64**, 587-590 (1990).
12. Ambegaokar, V., Eckern, U. & Schön, G. Quantum Dynamics of Tunneling between Superconductors. *Phys. Rev. Lett.* **48**, 1745-1748 (1982).
13. Leggett, A. J. et al. Dynamics of the dissipative two-state system. *Rev. Mod. Phys.* **59**, 1-85 (1987).
14. Weiss, U. *Quantum dissipative systems* (World Scientific and Singapore, 2012).
15. Aji, V. & Varma, C. M. Theory of the Quantum Critical Fluctuations in Cuprate Superconductors. *Phys. Rev. Lett.* **99**, 067003 (2007).
16. Chakravarty, S., Ingold, G.-L., Kivelson, S. & Luther, A. Onset of Global Phase Coherence in Josephson-Junction Arrays: A Dissipative Phase Transition. *Phys. Rev. Lett.* **56**, 2303-2306 (1986).
17. Fisher, M. P. A. Quantum Phase Slips and Superconductivity in Granular Films. *Phys. Rev. Lett.* **57**, 885-888 (1986).
18. Kapitulnik, A., Mason, N., Kivelson, S. A. & Chakravarty, S. Effects of dissipation on quantum phase transitions. *Phys. Rev. B* **63**, 125322 (2001).
19. Varma, C. M. Colloquium: Linear in temperature resistivity and associated mysteries including high temperature superconductivity. *Rev. Mod. Phys.* **92**, 031001 (2020).
20. Nagaosa, N. *Quantum Field Theory in Condensed Matter Physics* (Springer, New York, 1999).
21. Zwerger, W. Quantum effects and the resistive transition in superconducting granular films. *J. Low Temp. Phys.* **72**, 291-318 (1988).
22. Chakravarty, S. & Leggett, A. J. Dynamics of the Two-State System with Ohmic Dissipation. *Phys. Rev. Lett.* **52**, 5-8 (1984).
23. Beasley, M. R., Mooij, J. E. & Orlando, T. P. Possibility of Vortex-Antivortex Pair Dissociation in Two-Dimensional Superconductors. *Phys. Rev. Lett.* **42**,

- 1165-1168 (1979).
24. Lobb, C. J., Abraham, D. W. & Tinkham, M. Theoretical interpretation of resistive transition data from arrays of superconducting weak links. *Phys. Rev. B* **27**, 150-157 (1983).
 25. Sachdev, S. *Quantum Phase Transitions* (Cambridge Univ. Press, Cambridge, 2011).
 26. Millis, A. J. Effect of a nonzero temperature on quantum critical points in itinerant fermion systems. *Phys. Rev. B* **48**, 7183-7196 (1993).
 27. Vojta, T., Kotabage, C. & Hoyos, J. A. Infinite-randomness quantum critical points induced by dissipation. *Phys. Rev. B* **79**, 024401 (2009).
 28. Weiss, U. *Chapter 24 in Quantum dissipative systems* (Fourth Edition (World Scientific and Singapore), 2012).
 29. Shao, J. Dynamics of the spin-boson model at zero temperature and strong dissipation. *Phys. Rev. A* **105**, 052201 (2022).